Shap. Mem. Superelasticity (2022) 8:452–462
https://doi.org/10.1007/s40830-022-00400-2

TECHNICAL ARTICLE

Additive Manufacturing of Binary Ni–Ti Shape Memory Alloys Using Electron Beam Powder Bed Fusion: Functional Reversibility Through Minor Alloy Modification and Carbide Formation

P. Krooß[1] · C. Lauhoff[1] · T. Gustmann[2] · T. Gemming[2] · C. Sobrero[3] · F. Ewald[1] · F. Brenne[1,7] · T. Arold[1] · M. Nematolahi[4] · M. Elahinia[4] · J. Thielsch[5] · J. Hufenbach[2,6] · T. Niendorf[1]

Received: 5 September 2022 / Revised: 20 October 2022 / Accepted: 24 October 2022 / Published online: 30 November 2022

Abstract Shape memory alloys (SMAs), such as Ni–Ti, are promising candidates for actuation and damping applications. Although processing of Ni–Ti bulk materials is challenging, well-established processing routes (i.e. casting, forging, wire drawing, laser cutting) enabled application in several niche applications, e.g. in the medical sector. Additive manufacturing, also referred to as 4D-printing in this case, is known to be highly interesting for the fabrication of SMAs in order to produce near-net-shaped actuators and dampers. The present study investigated the impact of electron beam powder bed fusion (PBF-EB/M) on the functional properties of C-rich $Ni_{50.9}$-$Ti_{49.1}$ alloy. The results revealed a significant loss of Ni during PBF-EB/M processing. Process microstructure property relationships are discussed in view of the applied master alloy and powder processing route, i.e. vacuum induction-melting inert gas atomization (VIGA). Relatively high amounts of TiC, being already present in the master alloy and powder feedstock, are finely dispersed in the matrix upon PBF-EB/M. This leads to a local change in the chemical composition (depletion of Ti) and a pronounced shift of the transformation temperatures. Despite the high TiC content, superelastic testing revealed a good shape recovery and, thus, a negligible degradation in both, the as-built and the heat-treated state.

Keywords Shape memory alloy · Additive manufacturing · Superelasticity · Microstructure

Introduction

Shape memory alloys (SMAs) gained significant interest owing to their unique properties, e.g. shape memory effect (SME) and superelasticity (SE), which are based on a reversible phase transformation between a high-temperature austenitic and a low-temperature martensitic phase [1, 2]. Within the last decades, especially Ni–Ti SMAs (mainly binary alloys) received a lot of attention due to significant progresses in the fields of aerospace and the biomedical sector [3]. First and foremost, applications such as bone plates, screws for biomedical as well as stents for vasodilation applications, and medical equipment are known to represent Ni–Ti success stories in recent decades [4, 5].

Conventionally, the thermomechanical fabrication of Ni–Ti SMAs comprises melting of raw materials/elements (alloying), complex thermomechanical processing to form wires, plates or tubes and, finally, specific heat treatment and training for shape setting purposes and also adjusting the final transformation temperatures (TTs) [6]. One of the main issues in this regard is to control the chemical composition during the complete fabrication process.

✉ P. Krooß
krooss@uni-kassel.de

1 Institute of Materials Engineering, University of Kassel, 34125 Kassel, Germany

2 Leibniz Institute for Solid State and Materials Research Dresden, 01069 Dresden, Germany

3 Institute of Physics Rosario, CONICET- Universidad Nacional de Rosario, 2000 Rosario, Argentina

4 Mechanical, Industrial and Manufacturing Engineering Department, University of Toledo, Toledo, OH 43606, USA

5 Fraunhofer Institute for Machine Tools and Forming Technology IWU, 01187 Dresden, Germany

6 Institute of Materials Science, TU Bergakademie Freiberg, 09599 Freiberg, Germany

7 Infineon Technologies AG, 59581 Warstein, Germany

Besides controlling the Ni-content, carbon and oxygen pickups are well-known to heavily (element depletion due to secondary phase formation) affect the TTs in Ni–Ti SMAs [6, 7].

In recent years, additive manufacturing (AM) techniques, such as laser beam powder bed fusion of metals (PBF-LB/M) and electron beam powder bed fusion of metals (PBF-EB/M), came into focus of research, since solid metallic components can be directly fabricated from a computer-aided design (CAD) file by melting successive layers of a metallic powder feedstock [8–17]. AM techniques are also referred to as 3D-printing processes. In case a material is 3D-printed that is able to change its shape after printing, this being the case in SMAs, the term 4D-printing is used in literature and the public. Numerous studies were conducted in order to process Ni–Ti-based SMAs using PBF-LB/M [10, 11, 13, 17, 18]. Besides a substantial loss of Ni during processing stemming from the high local energy input, the impurity level of the initial feedstock material is already increased compared to the master alloy (conventional cast material/ingots) due to the processing and use of relative fine powder fractions (particle sizes below 150 µm), which have to be employed in powder-based AM. Hence, the TTs as well as the functional properties of additively manufactured Ni–Ti structures under both monotonic and cyclic loading are significantly affected and altered [19].

The necessity of Ni–Ti powder fabrication for AM processes like PBF-LB/M or PBF-EB/M will always cause a higher impurity level within this fabrication route [11, 20]. Powder atomization processes can mainly be divided into electrode induction melting gas atomization (EIGA), vacuum induction melting gas atomization (VIGA), plasma melting inert gas atomization (PIGA) as well as plasma rotating electrode processing atomization (PREP). Whereas the EIGA process uses induction coils to melt the pre-alloyed bulk material (crucible-free), the VIGA process relies mainly on graphite crucibles (or Al_2O_3) while the PIGA process utilizes a copper mold. All these details can affect the impurity level of the melt and, eventually, the manufactured powder (e.g. carbon or oxygen pickup) [11]. In addition to powder fabrication, many studies on additively manufactured Ni–Ti revealed that the appropriate choice of adequate process parameters (such as laser power, hatching distance, scanning speed and layer thickness) is crucial in order to adjust the microstructure for desired functional properties and to avoid a too pronounced Ni depletion during processing [11]. Most results shown in literature report on the evolution of microstructure of additively manufactured Ni–Ti or discuss the evolution of the TTs as a function of the process parameters as well as chemistry via differential scanning calorimetry (DSC). Furthermore, in many studies the functional properties of PBF-LB/M manufactured Ni–Ti samples, e.g. shape recovery in actuation and SE experiments have been investigated [10, 11, 13, 21–27]. It is noteworthy that the level of porosity (i.e. gas entrapments, lack of fusion defects and keyhole pores [28]) as well as stress-induced cracking, which often occurs concomitantly to the aforementioned aspects, must be carefully assessed during process optimization. The number of such defects needs to be decreased or fully avoided, respectively. In case many residual defects are present, more pronounced irreversibility and an inferior cyclic stability at higher strain amplitudes have to be expected for PBF-LB/M samples compared to conventional counterparts. Due to the fact that processing windows for obtaining dense PBF-LB/M parts remain small, a widespread commercial application of PBF-LB/M manufactured Ni–Ti has not been reported so far [11, 29, 30].

Only recently, PBF-EB/M was used in preliminary studies to process alloyed [14, 15], pre-mixed Ni–Ti powders [14, 15] and also pre-mixed powders [31] as well as wires [16]. Besides processing under vacuum atmosphere, one of the major advantages of PBF-EB/M (in contrast to PBF-LB/M) is the high process temperature usually applied. As a consequence, residual stresses (or cracking) can be avoided and impurity pickup during processing (mainly oxygen) kept at a minimum [12]. Zhou et al. [15] showed that the nickel and oxygen content is affected during PBF-EB/M processing. Following PBF-EB/M, the Ni-content decreased from 51.2 to 50.6 at.%, while the oxygen level increased by about 0.014 wt.% [15], which is rather weak in contrast to PBF-LB/M structures [21]. However, while Wang et al. [31] showed that the processing window in the PBF-EB/M process using pre-mixed powders is very narrow, limiting robust processing of dense parts, mechanical testing (additionally covered by DSC analysis) revealed functional (cyclic) properties even under tensile stress as well as high reversible strains (up to 10% in compression) in another study [15]. This clearly pinpoints the high potential of PBF-EB/M for AM of Ni–Ti SMAs. Furthermore, the microstructure was found to be different compared to well-known PBF-LB/M manufactured Ni–Ti SMAs [11, 15]. Recent studies demonstrate that upon PBF-EB/M of Ni–Ti strongly textured microstructures appear, which can be rationalized by epitaxial solidification [15, 16].

In order to address the impact of a carbon modified Ni–Ti master alloy on the functional properties of PBF-EB/M processed material, the present study focuses on PBF-EB/M processing of a Ni-rich Ni–Ti SMA ($Ni_{50.9}Ti_{49.1}$) featuring an increased carbon content (pronounced TiC formation), which originates from the as-cast material that has been processed to powder via the VIGA technique (high productivity and powder yield, respectively). Chemical and microstructural analysis were conducted in order to address the impact and evolution of impurities along the process

chain (as cast, powder, PBF-EB/M material) as well as the chemical composition on the functional material properties.

Experimental Details

$Ni_{50.9}Ti_{49.1}$ ingots with an increased carbon content of around 0.1 wt.% were provided in polycrystalline as-cast condition. The as-cast material was manufactured as a test batch by Ingpuls GmbH (Bochum, Germany) with a final composition of 50.94 at.% Ni (further element contents are listed as an inset in Fig. 1). The powder material with particle sizes ranging from 50 to 150 µm (d_{10} = 37 µm, d_{50} = 51 µm, d_{90} = 71 µm) was obtained via VIGA to exploit the higher output of finer particles and, thus, increased efficiency in contrast to EIGA and additional sieving (Nanoval GmbH & Co. KG, Berlin, Germany). The powder was kept under argon atmosphere until PBF-EB/M processing, which was conducted using an Arcam A2X machine (Arcam, Sweden). The build envelope was adjusted to 50 mm × 50 mm for reducing the overall powder consumption. X5CrNi18-10 steel was used for the build plate and samples were built without supports. The layer thickness was kept constant at 50 µm. Cuboids with a size of 10 mm × 10 mm × 10 mm were manufactured (beam current of 16 mA, acceleration voltage of 60 kV). A snake-like (bi-directional) scanning strategy, a scanning speed of 5000 mm/s and a hatching distance of 0.156 mm were applied at a process temperature of 920 °C. This parameter combination resulted in a volumetric energy density of 24.6 J/mm^3.

The transformation temperatures (TTs) were determined by differential scanning calorimetry (DSC) using a Mettler Toledo DSC-3 (for ingot and powder material) and a Perkin-Elmer DSC-8500 (for PBF-EB/M processed material, as-built condition) device at a heating and cooling rate of 10 °C/min. All samples were investigated by applying a minimum of two cycles (DSC-3: − 110 to 80 °C, DSC-8500: − 80 to 120 °C).

Generally, samples were tested in the as-built (i.e. without any post-process heat treatment) as well as in the solution heat-treated and aged condition (referred to as solutionized/aged in the remainder of the paper). For the solution heat treatment, samples were encapsulated in quartz tubes under argon atmosphere and heat-treated for 5.5 h at 950 °C followed by water quenching. Aging was conducted at 400 °C for 1.5 h after solution heat treatment.

The chemical compositions of the as-cast and powder material, including contaminants like Al, Co, Cu, Fe, as well as selected PBF-EB/M processed samples were determined using ICP-MS (inductively coupled plasma-mass spectrometry) and ICP-OES (inductively coupled plasma-optical emission spectroscopy) by Revierlabor GmbH (Essen, Germany). The carbon as well as oxygen and nitrogen contents were additionally analyzed by carrier gas hot extraction in reactive and helium atmosphere, respectively.

For initial microstructure analysis, samples were ground to a grit size of 5 µm and vibration-polished for 2.5 h with a 0.02 µm colloidal SiO_2 polishing suspension. Electron backscatter diffraction (EBSD) analysis, in order to capture the grain orientation and texture, as well as energy dispersive X-ray spectroscopy (EDS) for analyzing the local chemical composition were conducted using a scanning electron microscope (SEM, CamScan, Philipps). Furthermore, representative SEM images were used to determine

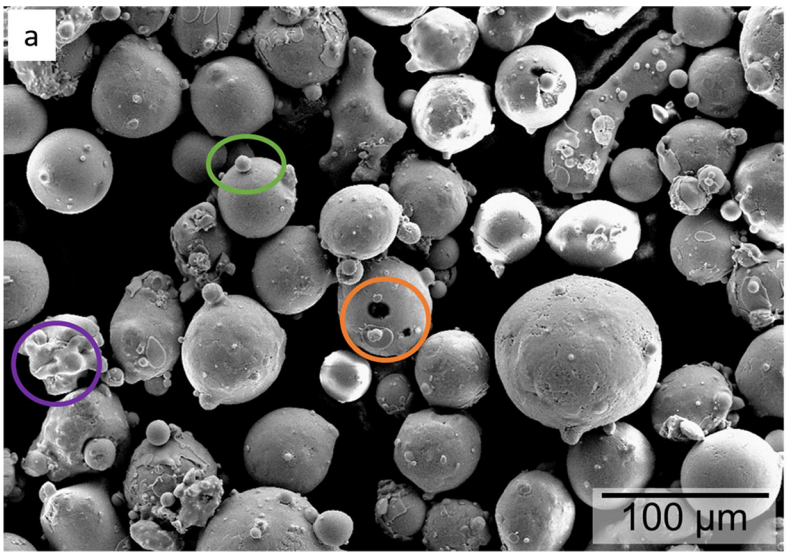

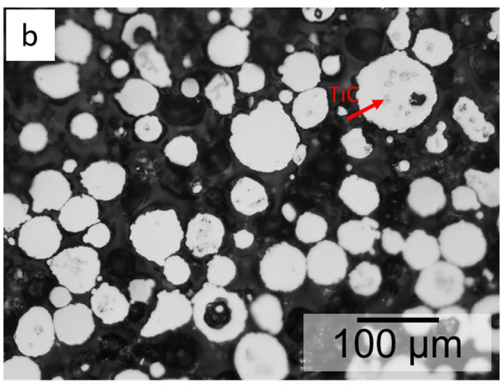

Element	As-cast (at.%)	Powder (at.%)	As-built (at.%)
Ni	50.94	50.12	48.88
Ti	49.05	48.14	49.68
O	< 0.01 wt.%	~ 0.1 wt.%	~ 0.1 wt.%
C	< 0.1 wt.%	~ 0.2 wt.%	~ 0.2 wt.%

Fig. 1 SEM image of the as-atomized powder in **a** and **b**. The inset table highlights the chemical compositions of the as-cast, powder and PBF-EB/M processed material. See main text for further details

the TiC area content. Selected subsets were calibrated (scale set) and analyzed using ImageJ 1.53t. At least three measurements were combined for subset (320 × 135 μm^2) analysis (Threshold-based). Transmission electron microscopy (TEM) analysis was carried out using a FEI Tecnai F30 operated at 300 kV.

X-ray diffraction (XRD) measurements were applied for phase analysis in each condition. A Seifert Analytical X-Ray diffractometer equipped with a Co tube and a monochromator was used operating at 40 kV and 35 mA. The crystallographic data for the indexed phases were taken from [32].

From the as-built cuboids 3 × 3 × 6 mm^3 compression samples were electro-discharged machined such that the longer (loading) axis was parallel to the build direction (BD). Samples were ground to a grit size of 5 µm for mechanical testing. Mechanical tests were conducted using a servo-hydraulic test frame. Quasi-static compression incremental strain tests (ISTs) at 50 °C were carried out in order to capture the SE response applying a strain rate of 1×10^{-3} s^{-1}. Heating of the samples was realized by controlled convection furnaces and temperatures were measured using a thermocouple directly attached to the sample surface. The strain was measured by an extensometer (gauge length 12 mm) directly attached to the compression grips, which were assumed to be fully rigid.

Results and Discussion

In the present work, the role of TiC on the functional properties of PBF-EB/M processed $Ni_{50.9}Ti_{49.1}$ is discussed, taking into account the entire processing route (i.e. initial ingots, powder, and additively manufactured material). Figures 1a and b depict SEM images of the powder particles and highlight (cf. the inset table) the chemical compositions of different material conditions, i.e. as-cast (ingot material), gas-atomized powder and the PBF-EB/M processed condition (as-built). From the micrograph in Fig. 1a, a spherical morphology can be deduced for the majority of the powder particles. Besides, very few non-spherical particles resulting from turbulences of the gas flow during gas atomization can be seen (e.g. within the purple circle, collided particles). Furthermore, satellites (green circle) as well as some few hollow particles (orange circle can be resolved. Figure 1b shows a representative SEM micrograph of the cross-section of particles. An EDS element mapping (not shown here) revealed the presence of TiC (see also Fig. 2) within some of the powder particles. This observation fits well with the determined chemical composition (see table in Fig. 1). The initial as-cast material features a relatively low, however, still significant carbon content, i.e. below 0.1 wt.%. In contrast, both powder and the PBF EB/M as-built material feature a higher amount of carbon, i.e. of about 0.2 wt.%. Consequently, the Ni–Ti material was additionally contaminated with carbon during the VIGA process due to the application of a graphite crucible, which supports the observation of the TiC precipitates in the powder material.

The analysis of the global chemical composition of the as-built PBF-EB/M condition (Fig. 1) reveals that due to the evaporation of Ni a Ti-rich Ni–Ti alloy is present and, thus, the precipitation of Ti_2Ni precipitates or Guinier–Preston (GP) zones can be expected upon artificial aging [11, 26, 27]. However, the EDS analysis of the as-built state in Fig. 2 proves that the local chemical composition differs significantly from the values obtained via ICP-OES (table in Fig. 1). From Fig. 2 it can be deduced that, as expected, the matrix is also composed of a high amount of finely dispersed TiC following PBF-EB/M processing. The sizes of the TiC particles in the as-built condition range from below 1 µm (Figs. 2a–c, 6) to above 10 µm (Fig. 2d–f) in diameter. Thus, due to the presence of carbon in the initial ingots as well as the further enrichment of carbon in the powder after VIGA, the local chemical composition of the PBF-EB/M material has changed: As a consequence of the TiC formation (TiC area content = 2.9 ± 0.3%), the matrix is not Ti-rich (see table in Fig. 1) but rather riched in Ni, leading to a decrease of the transformation temperatures [26]. In addition, the oxygen content increased during gas atomization (cf. Table in Fig. 1), which also results in a direct decrease of the TTs [26]. Zhou et al. [15] reported in their work that a slight oxygen pickup of about 0.01 wt.% occurred during PBF-EB/M processing of Ni–Ti. Thus, any substantial additional oxygen pickup stemming from the PBF-EB/M process can be excluded in present work.

Besides the TiC and oxygen content in the powder as well as in the as-built condition, another factor has to be considered. As already detailed before, the evaporation loss of Ni caused by the PBF-EB/M process contributes to changes of the global Ni content. As seen in the table of Fig. 1, due to the VIGA process the Ni-content decreased from the as-cast (50.94 at.%) to the powder material (50.12 at.%). Finally, the PBF-EB/M as-built material is characterized by a further significant depletion of Ni (to a final value of 48.88 at.%). This can be rationalized by the high process temperature, i.e. 920 °C, in combination with the vacuum atmosphere during processing, which promotes evaporation of elements like Ni [11, 12]. In total, approximately 1.2 at.% of Ni evaporated during PBF-EB/M processing. Considering this change solely, i.e. excluding the impact of the TiC and the oxygen content, TTs would increase [26]. However, the formation of TiC and the oxygen pickup clearly have the stronger impact here, eventually resulting in a decrease of the TTs, as will be shown in the following.

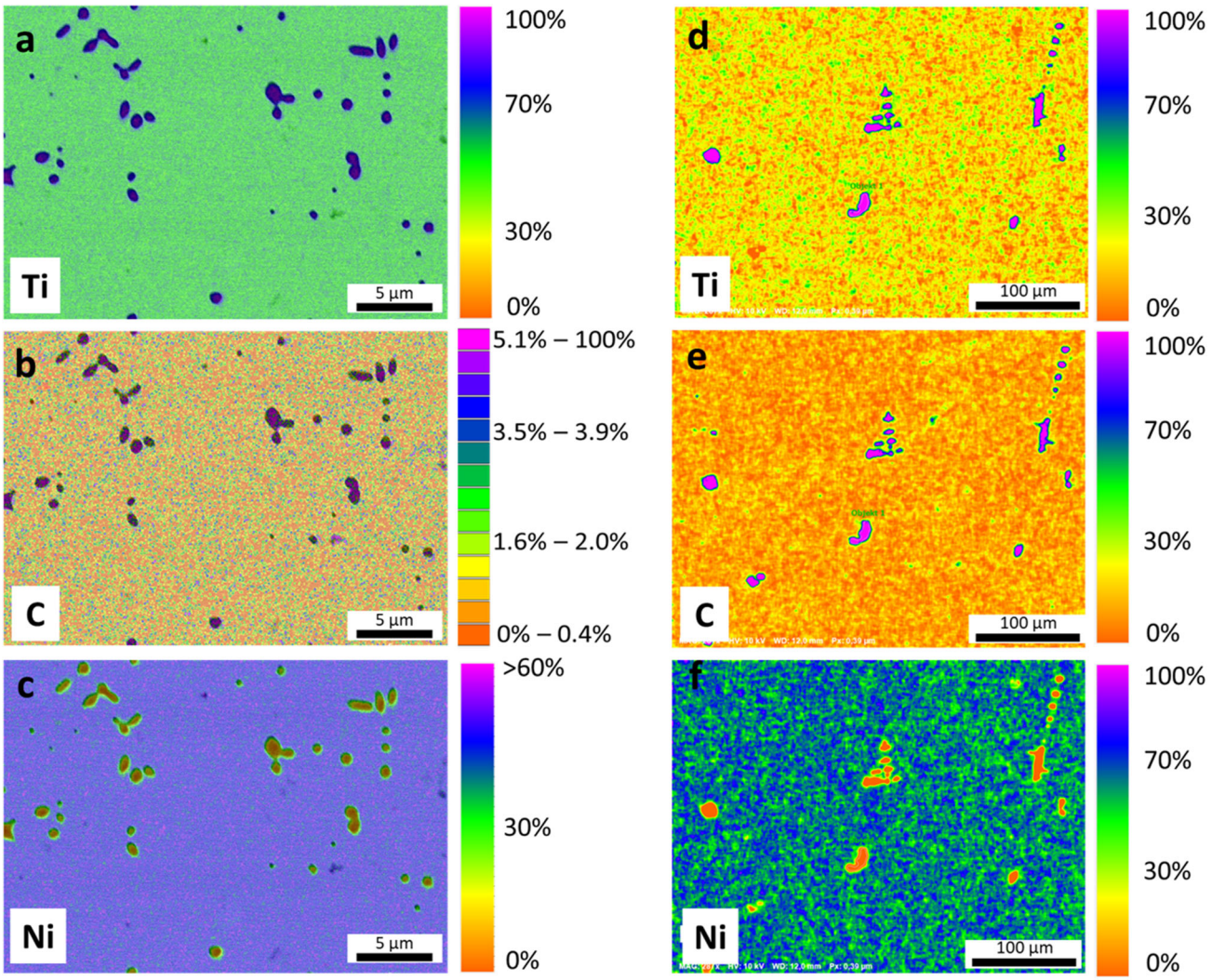

Fig. 2 EDS maps of PBF-EB/M processed Ni–Ti in the as-built condition revealing the presence of TiC in the microstructure at different length scales. Maps were obtained covering smaller (**a**–**c**) and larger (**d**–**f**) areas, respectively

Figure 3 depicts the evolution of the TTs obtained from the three material conditions, i.e. as-cast ingot material, powder and PBF-EB/M processed material in both as-built and solutionized/aged condition, via DSC analysis. Generally, the evolution of the TTs is in good agreement to the evolution of the Ni-content in the different material conditions. It has to be noted that the exothermic and endothermic reactions, which are associated with the forward (austenite to martensite and reverse martensite to austenite) transformation, respectively, can be clearly identified in the ingot material, the powder as well as the PBF-EB/M solutionized/aged condition. In contrast, in the PBF-EB/M as-built condition the peaks are significantly widened, what has been reported earlier for other materials as well [33, 34]. Reasons for this can be manifold, e.g. due to pronounced inhomogeneities in the microstructure following PBF EB/M. Thus, the complex microstructure in the as-built condition may hamper the thermal transformation behavior. Please also note, that due to this sluggish transformation behavior the martensite start (M_s) and finish (M_f temperatures were not determinable. However, further studies are crucially needed to characterize this in more detail. As detailed before, the increased carbon content can clearly be seen in the initial as-cast ingot material as well as in the powder. It is assumed that during PBF-EB/M the carbon content remains constant. The higher amount of carbon in the powder, which stems from the gas atomization process eventually further increasing the TiC content compared to the ingot material, should lead to a decrease of the TTs in the powder and consequently in both PBF-EB/M conditions as well. This is due to the fact that Ti is bond to the carbides and, thus, the Ni-content in the matrix is increased [27]. Instead of the decrease of the TTs, however, a significant increase is visible for the powder and PBF-

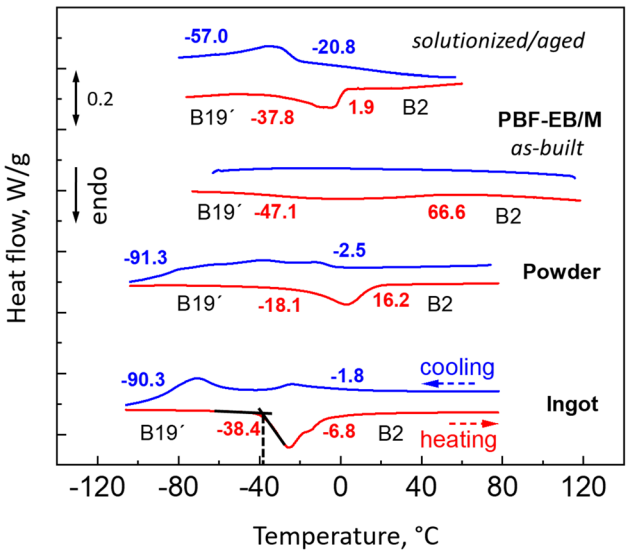

Fig. 3 DSC analysis different material conditions, i.e. PBF-EB/M (as-built and solutionized/aged), powder and as-cast ingot material

EB/M as-built material (Fig. 3), which can be explained by the Ni-loss upon both VIGA and PBF-EB/M processing [26].

Figure 4 depicts the microstructural constitution and evolution, respectively, obtained via EBSD analysis for the PBF-EB/M processed Ni–Ti in two different conditions, i.e. as-built and solutionized/aged. The inverse pole figure (IPF) orientation maps are plotted with respect to the BD (being from bottom to top in Fig. 4). A columnar grained microstructure with a strong ⟨001⟩ texture for both conditions is revealed. The maximum texture index was found to be 3.2 for the as-built and 6.3 for the solutionized/aged condition (Fig. 4c and d, respectively). As expected, following the heat treatment the microstructure only changes marginally, however, the texture index slightly increases. Highly textured and columnar grained microstructures can be very beneficial for improved functional properties (low residual strains due to reduced transformation constraints) in many SMAs [35–42]. Due to the strong anisotropic material properties of SMAs, a targeted microstructure design allows for a maximization of functional properties [35–42]. A recent study reporting on PBF-EB/M manufacturing of a Ni–Ti SMA also revealed similar columnar grained microstructures [15]. However, the microstructures shown in other studies focusing on Ni–Ti even feature a higher texture component in the ⟨001⟩-direction [15, 16]. Zhou et al. [15] comprehensively discussed the microstructural evolution of PBF-EB/M processed Ni–Ti. They explained that a strong influence of the processing parameters can be seen in the texture evolution

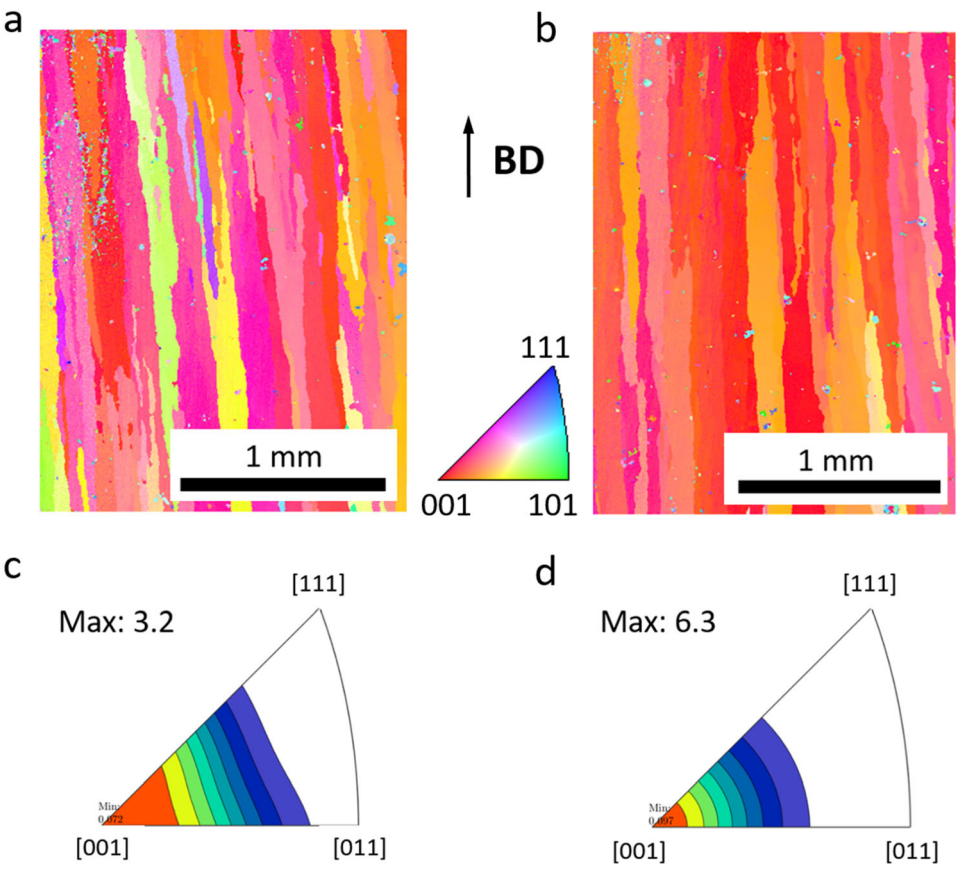

Fig. 4 EBSD IPF orientation maps (**a**, **b**) and IPFs (**c**, **d**) of PBF-EB/M processed Ni–Ti in the as-built (**a**, **c**) and solutionized/aged condition (**b**, **d**), respectively

as well as phase composition of the as-built condition [15]. Thus, the results of the current study, in general, support the findings of previous ones, i.e. PBFEB/M processing can result in strongly textured and columnar grained microstructures in Ni–Ti SMAs [15, 16]. Differences in the absolute values of the texture components between these studies eventually may be traced back to the applied process parameters (e.g. the scanning strategy) as well as to the amount of TiC in the different materials. Please note that an in-depth discussion of the impact of the process parameters used in the present study and in the studies being available in open literature [14, 15] cannot be realized at this point since not all relevant details about the applied process parameters are provided. Furthermore, Zhou et al. [15] used the PREP powder processing route in order to obtain a highly pure Ni–Ti powder feedstock [15]. The results in that study revealed only a carbon content of 0.036 wt.% in the powder material. Since the focus of the present study is to discuss the impact of an increased carbon content on the material properties, the role of the TiC precipitates needs to be discussed in detail in the following paragraphs.

Even though the global chemical composition is reduced in Ni, i.e. to a value of 48.88 at.% (see table in Fig. 1), the presence of the TiC particles leads to a local shift of the chemical composition, i.e. to a virtually increased Ni-content (Ti depletion of the matrix). In consequence, an aging treatment at 400 °C for 1.5 h is supposed to promote the precipitation of Ni_4Ti_3 at least in those local areas, where Ni is enriched due to the TiC particles [26]. In order to gain a deeper insight into the evolution and distribution of the TiC precipitates as well as on the formation of Ni_4Ti_3, analysis by XRD and TEM was conducted.

In Fig. 5b the result of an XRD phase analysis is depicted proofing the presence of the Ni_4Ti_3 precipitates in the solutionized/aged condition. In the as-built condition, in turn, the presence of the Ni_4Ti_3 precipitates cannot be confirmed via XRD analysis. Here, the microstructure seems to be composed solely of the austenitic phase according to the diffractogram (Fig. 5a). At this point, however, it should be mentioned that the presence of TiC (cf. Figs. 1 and 2) cannot be identified in the diffractograms for both the as-built as well as solutionized/aged condition. One explanation could be based on the volume fraction of the TiC particles, being not detectable via laboratory XRD instruments. Furthermore, it has to be noted that the strong (001) texture might affect the phase analysis via XRD. Differences in the peak intensities in the diffractograms of Fig. 5 can be associated with the slight differences in the texture intensities of both conditions (Fig. 4c and d). Zhou et al. [15] revealed that applying a process temperature of 750 °C in PBF-EB/M promotes the formation of Ni_4Ti_3 precipitates in an alloy featuring a nominal chemical composition of 51.3 at.% Ni and 48.7 at.% Ti. Besides the fact that Zhou et al. [15] used the PREP route for the powder manufacturing, which enables a significant lower carbon content, the higher PBF-EB/M process temperature (920 °C) in the present study may act as an *in-process* solution treatment for the alloy with slightly different chemical composition compared to [15]. This means that precipitation of Ni_4Ti_3 is only possible during cooling after the PBF-EB/M process is finished. The evolution of Ni_4Ti_3 will be discussed in more detail in the next paragraph.

In order to substantiate the argumentation on the evolution of the TiC and Ni_4Ti_3 precipitates, Fig. 6 shows the results of a TEM analysis of the PBF-EB/M processed material in both conditions, i.e. as-built and solutionized/aged. From the micrographs shown (Fig. 6a and b) it can be deduced that TiC is present in the material. The distribution of the TiC particles seems to be dispersed throughout the samples/cross-sections. This fact strengthens the

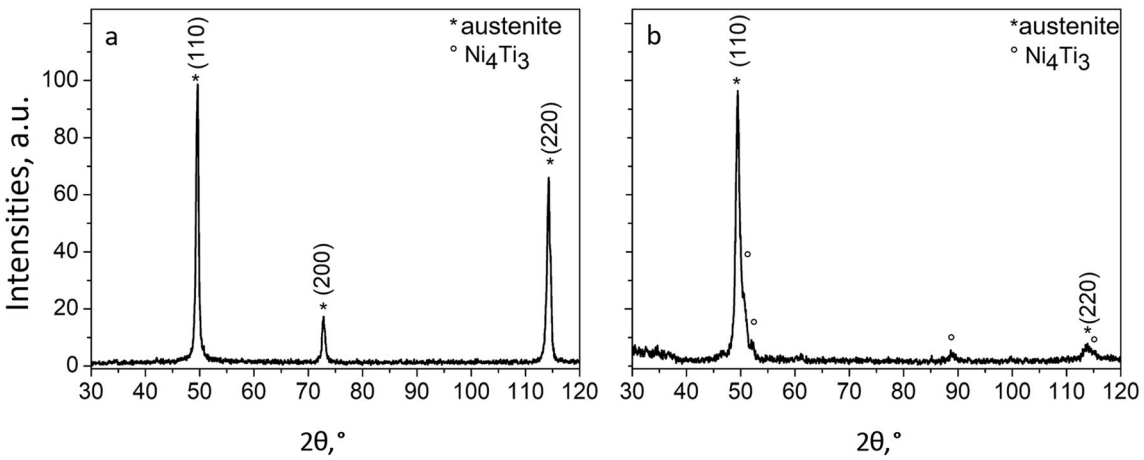

Fig. 5 XRD intensity plots for PBF-EB/M-processed Ni–Ti in the as-built (**a**) and solutionized/aged condition (**b**), respectively

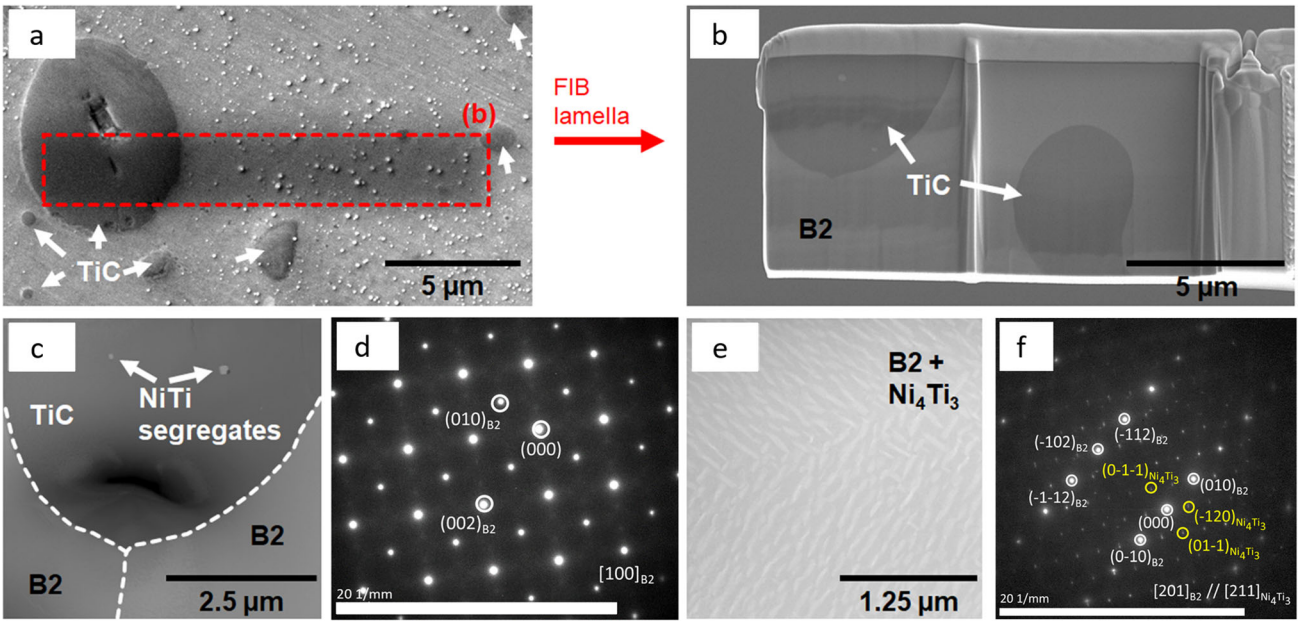

Fig. 6 Microstructural analysis of PBF-EB/M processed Ni–Ti. SEM overview of an as-built sample (**a**) and the extracted FIB lamellae (**b**). The white arrows highlight the presence of TiC. TEM analysis of the as-built sample shown in (**c**). Diffraction analysis of the as-built condition is depicted in (**d**). TEM bright field image of a solutionized/aged condition in (**e**) and diffraction analysis (**f**) of the microstructure shown in (**e**)

argumentation of the previous chapter, i.e. dispersed TiC increase the Ni-content in the matrix (Fig. 2). It is noteworthy that TiC precipitates formed in two different length-scales, i.e. in the range of 1 – 10 µm and in a submicron range (Figs. 1, 2 and 6a).

Considering the evolution of the Ni_4Ti_3 precipitates, differences are seen between both sample states. Results of the XRD analysis (Fig. 5) already discussed before indicated that Ni_4Ti_3 precipitates were only formed in the solutionized/aged condition, while the as-built condition did not show additional phases that formed during PBF-EB/M processing. The diffraction studies obtained from TEM confirm these results. Only B2 austenite and TiC (the latter not resolved by XRD) are found in the as-built matrix (Fig. 6a–d). This correlates well with the applied processing temperature of 920 °C (being effective as an *in-process* solution treatment for each processed layer). However, one would expect that during cooling of the build chamber additional phases form according to the Ni–Ti binary phase diagram. Figure 7 depicts the measured temperature-time cooling path within the build chamber following PBF-EB/M processing plotted in a schematic Time–Temperature-Transformation (TTT) diagram for a Ni-rich Ni–Ti SMA. Although the chemical composition of the material in the present study obviously differs from the one used to create the TTT plot [43], i.e. 52 at.% Ni, a qualitative comparison seems still to be reasonable. Following PBF-EB/M processing at 920 °C, the build chamber needs to cool down, which can take several hours depending on the size of the

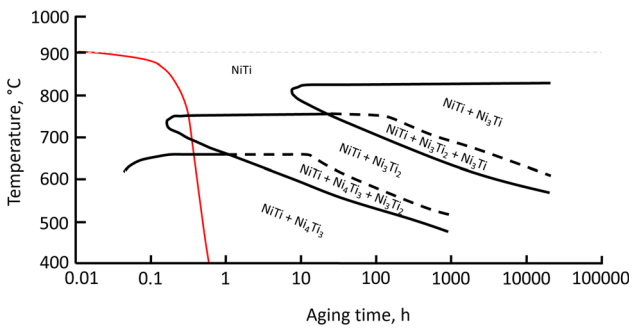

Fig. 7 Schematic TTT diagram depicting the cooling path of the build chamber following PBF-EB/M processing (recompiled from [43])

build envelope and the number of samples placed within it. Regarding Fig. 7, only the relevant temperature window for precipitation processes (900 °C to 400 °C) is highlighted and it can be deduced that the temperature of the as-built material crosses two main precipitation areas, i.e. Ni_3Ti_2 at around 750 °C and Ni_4Ti_3 at around 650 °C, during the post-process cooling path. According to Fig. 7, one would expect the precipitation of Ni_4Ti_3 and/or Ni_3Ti_2. However, as it was confirmed via XRD and TEM analysis (Figs. 5 and 6a–d, respectively) the formation of Ni_4Ti_3 precipitates seems to be suppressed following cooling in the PBF-EB/M machine. One explanation could be that during cooling in the relevant time–temperature window from 900 to 400 °C the precipitation of Ni_4Ti_3 particles is not favored due to the presence of a relative high amount of

TiC [44]. In a very recent study, Zhang et al. [44] processed a mixture of Ni–Ti (Ni_{60}–Ti_{40} wt.%) and TiC powders via directed energy deposition. They revealed that the addition of TiC to a binary Ni–Ti alloy leads to a restriction of the Ni_4Ti_3 precipitation nucleation and growth [44]. Therefore, it is most likely that the presence of TiC in the present study hampers the precipitation of Ni_4Ti_3 during cooling from the PBF-EB/M processing temperature and the dwell time in a specific aging window seems not be sufficient. Following artificial aging at 400 °C for 1.5 h, however, it is obvious that the time–temperature combination is well-suited to allow for the precipitation of Ni_4Ti_3, as can be seen from Figs. 5 and 6e and f.

Figure 8 depicts the compressive SE stress–strain hysteresis following PBF-EB/M processing. Both investigated sample conditions, i.e. as-built (Fig. 8a) and solutionized/aged (Fig. 8b), show a remarkable SE response with a high strain reversibility during ISTs up to a maximum applied compressive strain of -6%. Differences are seen in the critical stress for the stress-induced martensitic transformation (SIMT), being around 850 MPa for the as-built condition (Fig. 8a) and 550 MPa for the solutionized/aged state (Fig. 8b). Obviously, the different stresses can be linked to the thermal post-treatment and, thus, to changes

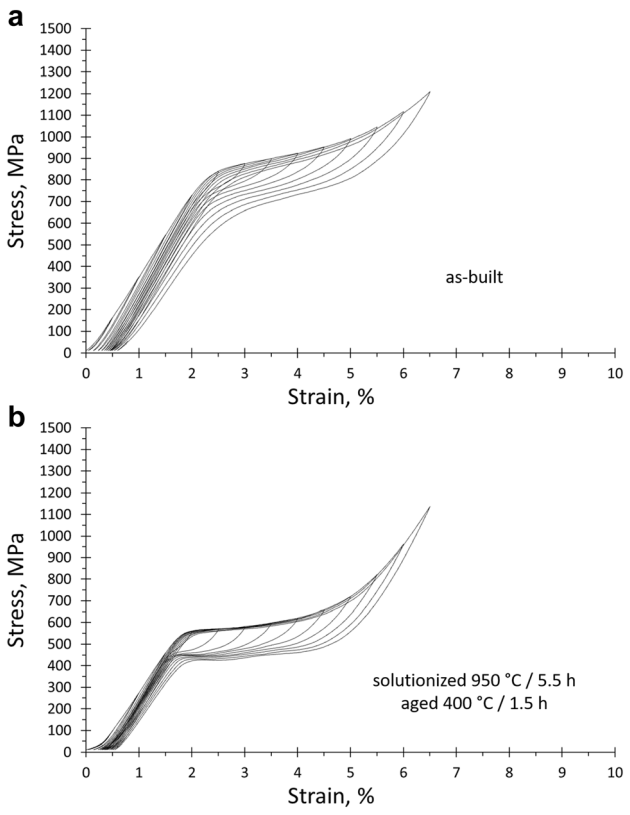

Fig. 8 Superelastic stress–strain response of PBF-EB/M processed Ni–Ti in the as-built (**a**) and solutionized/aged condition (**b**) obtained at 50 °C. Loading direction was parallel to the BD

in the phase composition of the conditions and consequently to a change in the TTs as discussed in the previous paragraphs. Comparing the as-built and solutionized/aged condition, the volume fraction and size of evolving precipitates dictate the functional properties in the two different material conditions, i.e. TTs as well as coherency stresses are affected in the solutionized/aged condition. The TEM analysis (Fig. 6a–d) did not reveal any presence of Ni_4Ti_3 precipitates in the as-built condition, which is also supported by the XRD analysis (Fig. 5a). In comparison, following a solutionizing and aging heat treatment the volume fraction of Ni_4Ti_3 precipitates clearly increased as revealed by, as can be seen from Figs. 5 and 6e and f, showing the presence of a third phase (besides austenite and TiC). Their presense significantly affect the critical stress for SIMT as well as stress hysteresis and reversibility [37, 38]. In other words, both the increase of the TTs due to the formation of Ni-rich precipitates in the B2 matrix and the formation of coherency stress fields around these precipitates, support the SIMT, i.e. the critical stress for SIMT is decreased. This fact also promotes the higher and almost degradation-free strain reversibility of the solutionized/aged condition (Fig. 8b).

Finally, it can be stated that the enrichment of Ni in the matrix, being related to the formation of TiC in the initial material ingot as well as to a further enrichment in the VIGA process (Figs.1, 2), dominates the microstructural evolution as well as the functional properties. It is obvious that due to the presence of TiC precipitates in the matrix, a Ni-loss during PBF-EB/M processing has been compensated. The formation of Ni_4Ti_3 precipitates seems to be generally preferred upon artificial aging. In contrast to the intrinsic post-process heat treatment, i.e. relatively slow cooling from the build temperature of 920 °C, the solutionizing and aging treatment at 400 °C for 1.5 h leads to the formation of a significant volume fraction of Ni_4Ti_3 precipitates (Figs. 5b and 6e and f). However, even in the as-built condition without conducting a specific post-process heat treatment and in absence of any Ni_4Ti_3 precipitates, promising functional properties are seen in the present study, which has not been reported for additively manufactured Ni–Ti so far. However, it is important to note at this point that the austenite finish temperature (A_f) of the as-built condition is around 60 °C and, thus, fully reversibly SE material properties cannot be expected due to the thermal instability of the martensite at the test temperature of 50 °C. After solutionizing at 950 °C and aging for 1.5 h at 400 °C, a shape recovery of nearly 100% has been finally observed (Fig. 8b). The formation of fine coherent Ni_4Ti_3 precipitates is well-known to be beneficial for the functional properties [45]. Thus, although a high amount of TiC is present in the matrix in both conditions, the formation of dispersed Ni_4Ti_3 precipitates in the

solutionized/aged condition seems to significantly improve the material response. In recent studies reporting on the mechanical response of PBF-EB/M processed Ni–Ti, a high strain reversibility has been presented in absence of the here reported significant volume fraction of TiC [14–16]. In those studies, the authors reported reversible strains up to 10% (low carbon content, as-built) under tensile load. The considered Ni–Ti material features only limited inclusions compared to the current study due to the PREP powder processing route [15]. In the present work, around -6% reversible compressive strains could be observed even though TiC are present in the matrix. It should be noted that these high reversible strains, with respect to the aforementioned [15] and the present study, can be linked to the synergetic interplay of the general anisotropic material behavior of Ni–Ti and the columnar grained microstructure in the PBF-EB/M processed Ni–Ti. Furthermore, the VIGA process seems to be obviously well-suited for the fabrication of more cost-effective and low-purity Ni–Ti SMAs, since the Ni-loss can be compensated by finely dispersed TiC, eventually maintaining functional reversibility.

Conclusion

The results of the current study can be summarized as follows:

- C-rich $Ni_{50.9}Ti_{49.1}$ (at.%) SMA powder (C-content = 0.2 wt.%) was successfully processed using the PBF-EB/M technique.
- After PBF-EB/M of the C-rich Ni-Ti TiC particles were dispersed in the Ni–Ti matrix of processing the as-built and solutionized/aged condition. Such kind of microstructure evolution enabled an effective compensation of the Ni-loss during PBF-EB/M manufacturing since Ti was bond in the carbides. In consequence, the matrix was enriched in Ni.
- Whereas artificial aging led to the formation of Ni_4Ti_3 precipitates, no significant precipitation of Ni-rich phases could be detected in the as-built state.
- Even in the as-built condition, promising functional material properties were observed. Finally, upon artificial solutionizing and aging, Ni_4Ti_3 precipitates formed in the material and a superior SE reversibility was obtained.

Acknowledgements Financial support by Deutsche Forschungsgemeinschaft (DFG) under Project Number 398899207 is gratefully acknowledged. The assistance of Dr.-Ing. Frank Zeismann in SEM work is gratefully acknowledged. T. Gustmann and J. Thielsch are grateful for financial support (e.g. powder material) by Fraunhofer Cluster of Excellence Programmable Materials (FCPM, project title: "Generativ gefertigte metallische Metamaterialien"). T. Gustmann, T. Gemming and J. Hufenbach thank B. Bartusch, M. Seifert, D. Bieberstein and T. Wiek for technical assistance as well as A. Voß, A. Voidel and H. Bußkamp for the chemical analysis.

Funding Open Access funding enabled and organized by Projekt DEAL.

Data Availability The data that support the findings of this study are available from the corresponding author upon reasonable request.

References

1. Lagoudas DC (2008) Shape memory alloys. Springer, US, Boston, MA
2. Otsuka K (ed) (1999) Shape memory materials, 1st edn. Cambridge Univ. Press, Cambridge
3. Sehitoglu H, Patriarca L, Wu Y (2017) Shape memory strains and temperatures in the extreme. Curr Opin Solid State Mater Sci 21(2):113–120
4. Machado LG, Savi MA (2003) Medical applications of shape memory alloys. Braz J Med Biol Res 36(6):683–691
5. Pfeifer R, Müller CW, Hurschler C, Kaierle S, Wesling V, Haferkamp H (2013) Adaptable orthopedic shape memory implants. Procedia CIRP 5:253–258
6. Otsuka K, Ren X (2005) Physical metallurgy of Ti–Ni-based shape memory alloys. Prog Mater Sci 50(5):511–678
7. Firstov G, van Humbeeck J, Koval Y (2004) High-temperature shape memory alloys. Mater Sci Eng, A 378(1–2):2–10
8. Safaei K, Abedi H, Nematollahi M, Kordizadeh F, Dabbaghi H, Bayati P et al (2021) Additive manufacturing of NiTi shape memory alloy for biomedical applications: review of the LPBF process ecosystem. JOM 73:3771–3786
9. Farjam N, Nematollahi M, Andani MT, Mahtabi MJ, Elahinia M (2020) Effects of size and geometry on the thermomechanical properties of additively manufactured NiTi shape memory alloy. Int J Adv Manuf Technol 107(7–8):3145–3154
10. Alagha AN, Hussain S, Zaki W (2021) Additive manufacturing of shape memory alloys: a review with emphasis on powder bed systems. Mater Des 204:109654
11. Elahinia M, Shayesteh Moghaddam N, Taheri Andani M, Amerinatanzi A, Bimber BA, Hamilton RF (2016) Fabrication of NiTi through additive manufacturing: a review. Prog Mater Sci 83:630–663
12. Körner C (2016) Additive manufacturing of metallic components by selective electron beam melting—a review. Int Mater Rev 61(5):361–377
13. Elahinia MH, Hashemi M, Tabesh M, Bhaduri SB (2012) Manufacturing and processing of NiTi implants: a review. Prog Mater Sci 57(5):911–946

14. Hayat MD, Chen G, Liu N, Khan S, Tang HP, Cao P (2018) Physical and tensile properties of NiTi alloy by selective electron beam melting. KEM 770:148–154
15. Zhou Q, Hayat MD, Chen G, Cai S, Qu X, Tang H et al (2019) Selective electron beam melting of NiTi: microstructure, phase transformation and mechanical properties. Mater Sci Eng A 744:290–298
16. Dutkiewicz J, Rogal Ł, Kalita D, Kawałko J, Węglowski MS, Kwieciński K et al (2021) Microstructure, mechanical properties, and martensitic transformation in NiTi shape memory alloy fabricated using electron beam additive manufacturing technique. J. Materi Eng Perform 31:1609–1621
17. Khoo ZX, Liu Y, An J, Chua CK, Shen YF, Kuo CN (2018) A review of selective laser melted NiTi shape memory alloy. Materials (Basel, Switzerland) 11(4):519
18. Gustmann T, Gutmann F, Wenz F, Koch P, Stelzer R, Drossel W-G et al (2020) Properties of a superelastic NiTi shape memory alloy using laser powder bed fusion and adaptive scanning strategies. Prog Addit Manuf 5(1):11–18
19. Bagheri A, Mahtabi MJ, Shamsaei N (2018) Fatigue behavior and cyclic deformation of additive manufactured NiTi. J Mater Process Technol 252:440–453
20. Saedi S, Saghaian SE, Jahadakbar A, Shayesteh Moghaddam N, Taheri Andani M, Saghaian SM et al (2018) Shape memory response of porous NiTi shape memory alloys fabricated by selective laser melting. J Mater Sci 29(4):40
21. Haberland C, Elahinia M, Walker JM, Meier H, Frenzel J (2014) On the development of high quality NiTi shape memory and pseudoelastic parts by additive manufacturing. Smart Mater Struct 23(10):104002
22. Shayesteh Moghaddam N, Saedi S, Amerinatanzi A, Hinojos A, Ramazani A, Kundin J et al (2019) Achieving superelasticity in additively manufactured NiTi in compression without post-process heat treatment. Sci Rep 9(1):41
23. Hamilton RF, Palmer TA, Bimber BA (2015) Spatial characterization of the thermal-induced phase transformation throughout as-deposited additive manufactured NiTi bulk builds. Scripta Mater 101:56–59
24. Bormann T, Müller B, Schinhammer M, Kessler A, Thalmann P, de Wild M (2014) Microstructure of selective laser melted nickel–titanium. Mater Charact 94:189–202
25. Xue L, Atli KC, Picak S, Zhang C, Zhang B, Elwany A et al (2021) Controlling martensitic transformation characteristics in defect-free NiTi shape memory alloys fabricated using laser powder bed fusion and a process optimization framework. Acta Mater 215:117017
26. Frenzel J, George EP, Dlouhy A, Somsen C, Wagner M-X, Eggeler G (2010) Influence of Ni on martensitic phase transformations in NiTi shape memory alloys. Acta Mater 58(9):3444–3458
27. Frenzel J, Zhang Z, Somsen C, Neuking K, Eggeler G (2007) Influence of carbon on martensitic phase transformations in NiTi shape memory alloys. Acta Mater 55(4):1331–1341
28. Zerbst U, Bruno G, Buffiere J-Y, Wegener T, Niendorf T, Wu T et al (2021) Damage tolerant design of additively manufactured metallic components subjected to cyclic loading: State of the art and challenges. Prog Mater Sci 121:100786
29. Dadbakhsh S, Speirs M, van Humbeeck J, Kruth J-P (2016) Laser additive manufacturing of bulk and porous shape-memory NiTi alloys: from processes to potential biomedical applications. MRS Bull 41(10):765–774
30. Khademzadeh S, Carmignato S, Parvin N, Zanini F, Bariani PF (2016) Micro porosity analysis in additive manufactured NiTi parts using micro computed tomography and electron microscopy. Mater Des 90:745–752
31. Wang C, Tan XP, Du Z, Chandra S, Sun Z, Lim C et al (2019) Additive manufacturing of NiTi shape memory alloys using premixed powders. J Mater Process Technol 271:152–161
32. Tirry W, Schryvers D, Jorissen K, Lamoen D (2006) Quantitative determination of the crystal structure of Ni_4Ti_3 precipitates. Mater Sci Eng, A 438–440:517–520
33. Kireeva IV, Pons J, Picornell C, Chumlyakov Y, Cesari E, Kretinina IV (2013) Influence of γ' nanometric particles on martensitic transformation and twinning structure of L10 martensite in Co–Ni–Ga ferromagnetic shape memory single crystals. Intermetallics 35:60–66
34. Lauhoff C, Fischer A, Sobrero C, Liehr A, Krooß P, Brenne F et al (2020) Additive manufacturing of Co-Ni-Ga high-temperature shape memory alloy: processability and phase transformation behavior. Metall Mater Trans A 51(3):1056–1061
35. Omori T, Kusama T, Kawata S, Ohnuma I, Sutou Y, Araki Y et al (2013) Abnormal grain growth induced by cyclic heat treatment. Science 341(6153):1500–1502
36. Omori T, Iwaizako H, Kainuma R (2016) Abnormal grain growth induced by cyclic heat treatment in Fe-Mn-Al-Ni superelastic alloy. Mater Des 101:263–269
37. Ueland SM, Chen Y, Schuh CA (2012) Oligocrystalline shape memory alloys. Adv Funct Mater 22(10):2094–2099
38. Ueland SM, Schuh CA (2012) Superelasticity and fatigue in oligocrystalline shape memory alloy microwires. Acta Mater 60(1):282–292
39. Ueland SM, Schuh CA (2013) Grain boundary and triple junction constraints during martensitic transformation in shape memory alloys. J Appl Phys 114(5):53503
40. Vollmer M, Krooß P, Segel C, Weidner A, Paulsen A, Frenzel J et al (2015) Damage evolution in pseudoelastic polycrystalline Co–Ni–Ga high-temperature shape memory alloys. J Alloy Compd 633:288–295
41. Lauhoff C, Vollmer M, Krooß P, Kireeva I, Chumlyakov YI, Niendorf T (2019) pathways towards grain boundary engineering for improved structural performance in polycrystalline Co–Ni–Ga shape memory alloys. Shap Mem Superelast 5(1):73–83
42. Lauhoff C, Sommer N, Vollmer M, Mienert G, Krooß P, Böhm S et al (2020) Excellent superelasticity in a Co-Ni-Ga high-temperature shape memory alloy processed by directed energy deposition. Mater Res Lett 8(8):314–320
43. Nishida M, Wayman CM, Honma T (1986) Precipitation processes in near-equiatomic TiNi shape memory alloys. MTA 17(9):1505–1515
44. Zhang D, Li Y, Wang H, Cong W (2021) An investigation on Ni_4Ti_3 phase precipitation and its effects in laser directed energy deposition of TiC–NiTi composites. Mater Sci Eng, A 809:140976
45. Gall K, Maier H (2002) Cyclic deformation mechanisms in precipitated NiTi shape memory alloys. Acta Mater 50(18):4643–4657